Anisotropic spin model of strong spin-orbit-coupled triangular antiferromagnets

Yao-Dong Li,[1] Xiaoqun Wang,[2] and Gang Chen[3,4,*]

[1]*School of Computer Science, Fudan University, Shanghai 200433, People's Republic of China*

[2]*Department of Physics and Astronomy, Innovative Center for Advanced Microstructures, Shanghai Jiao Tong University, Shanghai 200240, People's Republic of China*

[3]*State Key Laboratory of Surface Physics, Center for Field Theory and Particle Physics, Department of Physics, Fudan University, Shanghai 200433, People's Republic of China*

[4]*Collaborative Innovation Center of Advanced Microstructures, Nanjing 210093, People's Republic of China*

(Received 18 April 2016; revised manuscript received 12 June 2016; published 5 July 2016)

Motivated by the recent experimental progress on the strong spin-orbit-coupled rare-earth triangular antiferromagnet, we analyze the highly anisotropic spin model that describes the interaction between the spin-orbit-entangled Kramers' doublet local moments on the triangular lattice. We apply the Luttinger-Tisza method, the classical Monte Carlo simulation, and the self-consistent spin wave theory to analyze the anisotropic spin Hamiltonian. The classical phase diagram includes the 120° state and two distinct stripe-ordered phases. The frustration is very strong and significantly suppresses the ordering temperature in the regimes close to the phase boundary between two ordered phases. Going beyond the semiclassical analysis, we include the quantum fluctuations of the spin moments within a self-consistent Dyson-Maleev spin-wave treatment. We find that the strong quantum fluctuations melt the magnetic order in the frustrated regions. We explore the magnetic excitations in the three different ordered phases as well as in strong magnetic fields. Our results provide a guidance for the future theoretical study of the generic model and are broadly relevant for strong spin-orbit-coupled triangular antiferromagnets such as $YbMgGaO_4$, RCd_3P_3, RZn_3P_3, RCd_3As_3, RZn_3As_3, and $R_2O_2CO_3$.

DOI: 10.1103/PhysRevB.94.035107

I. INTRODUCTION

Since the discovery of topological insulator [1], spin-orbit coupling (SOC) has become one of the central topics in modern condensed matter physics. While topological insulator is the band structure topological property of noninteracting electrons, the interplay of strong spin-orbit coupling and strong electron correlation is one of the central questions in the field of strong correlation physics [2]. In recent years, there has been intense interest and activities in the heavy-element-based materials where both strong spin-orbit coupling and strong electron correlations are present. The spin-orbit entanglement in strongly correlated electron systems can give rise to unprecedented and realistic models that may support novel phases and phenomena.

Magnets with rare earth elements are natural physical systems to search for strong correlation physics with strong SOC. In the rare-earth magnets, the correlation is often quite strong and the $4f$ electrons are very localized. The atomic spin-orbit coupling entangles the spin and orbital angular momenta and leads to spin-orbit-entangled local moments. Recently, a Ytterbium-based rare-earth magnet, $YbMgGaO_4$, has been synthesized and characterized [3,4]. The magnetic ions, Yb^{3+}, form a perfect triangular lattice. The SOC and the crystal electric field together lead to a Kramers' doublet for the Yb^{3+} ion. This Kramers' doublet is described by an effective spin-1/2 local moment. The thermodynamic and NMR measurements found that the system remains disordered down to 60 mK [3]. More recently, another rare-earth triangular antiferromagnet $CeCd_3P_3$ was studied experimentally [5]. Although this material remains paramagnetic down to 0.48 K and this temperature is probably not very low by the $4f$ electrons' standard, as we show in Table I, $CeCd_3P_3$, together with the rare-earth oxycarbonates $R_2O_2CO_3$, represents a new family of rare-earth triangular antiferromagnets that need further investigation [5–8]. Like the Yb^{3+} ion in $YbMgGaO_4$, the Ce^{3+} ion in $CeCd_3P_3$ experiences the same D_{3d} crystal field and is also described by an effective spin-1/2 Kramers doublet [5]. Partly motivated by these experiments, in this paper we consider the generic spin model that generally describes the spin-orbit-entangled Kramers' doublets on the triangular lattice and study the magnetic phase diagram and the magnetic excitation of this new model.

Due to the spin-orbit-entangled nature of the Kramers' doublets, the interaction between the effective spin-1/2 moments is *anisotropic* both in the effective spin space and in the position space [2,10–16]. Therefore, the spin interaction depends on the bond orientations. This is one of the key properties of the strong spin-orbit-coupled magnets. The most generic spin Hamiltonian allowed by the space group symmetry of the rare-earth triangular system is given by [3]

$$\begin{aligned}\mathcal{H} = &\sum_{\langle ij\rangle} J_{zz} S_i^z S_j^z + J_{\pm}(S_i^+ S_j^- + S_i^- S_j^+) \\ &+ J_{\pm\pm}(\gamma_{ij} S_i^+ S_j^+ + \gamma_{ij}^* S_i^- S_j^-) \\ &- \frac{i J_{z\pm}}{2}[(\gamma_{ij}^* S_i^+ - \gamma_{ij} S_i^-) S_j^z \\ &+ S_i^z(\gamma_{ij}^* S_j^+ - \gamma_{ij} S_j^-)], \end{aligned} \tag{1}$$

where $S_i^{\pm} = S_i^x \pm i S_i^y$ and $\gamma_{ij} = \gamma_{ji} = 1, e^{i2\pi/3}, e^{-i2\pi/3}$ are the phase factors for the bond ij along the $\mathbf{a_1}, \mathbf{a_2}, \mathbf{a_3}$ directions, respectively (see Fig. 1). The first line of Eq. (1) is the standard XXZ model and is invariant under the global spin rotation

*gchen_physics@fudan.edu.cn

TABLE I. A list of rare-earth triangular antiferromagnets. Note the Curie-Weiss temperatures (Θ_{CW}) for the second to the sixth compounds are obtained from the magnetic susceptibility measurments above 50 K. Here, "PM" refers to paramagnetic and "AFM" refers to antiferromagnetic. The frustration parameter f is defined in Sec. III B.

Compound	Magnetic ion	Space group	Local moment	Θ_{CW} (K)	Magnetic transition	Frustration para. f	Refs.
$YbMgGaO_4$	$Yb^{3+}(4f^{13})$	$R\bar{3}m$	Kramers doublet	-4	PM down to 60 mK	$f > 66$	[4]
$CeCd_3P_3$	$Ce^{3+}(4f^1)$	$P6_3/mmc$	Kramers doublet	-60	PM down to 0.48 K	$f > 200$	[5]
$CeZn_3P_3$	$Ce^{3+}(4f^1)$	$P6_3/mmc$	Kramers doublet	-6.6	AFM order at 0.8 K	$f = 8.2$	[7]
$CeZn_3As_3$	$Ce^{3+}(4f^1)$	$P6_3/mmc$	Kramers doublet	-62	Unknown	Unknown	[8]
$PrZn_3As_3$	$Pr^{3+}(4f^2)$	$P6_3/mmc$	Non-Kramers doublet	-18	Unknown	Unknown	[8]
$NdZn_3As_3$	$Nd^{3+}(4f^3)$	$P6_3/mmc$	Kramers doublet	-11	Unknown	Unknown	[8]
$Nd_2O_2CO_3$	$Nd^{3+}(4f^3)$	$P6_3/mmc$	Kramers doublet	-21.7	AFM order at 1.25 K	$f = 17.4$	[9]
$Sm_2O_2CO_3$	$Sm^{3+}(4f^5)$	$P6_3/mmc$	Kramers doublet	-18	AFM order at 0.61 K	$f = 31$	[9]
$Dy_2O_2CO_3$	$Dy^{3+}(4f^9)$	$P6_3/mmc$	Kramers doublet	-10.6	AFM order at 1.21 K	$f = 8.8$	[9]

around the z direction. Here we have chosen the coordinate system for the spin components to be identical with the one for the position space (see Fig. 1). The $J_{\pm\pm}$ and $J_{z\pm}$ terms of Eq. (1) define the anisotropic interactions that arise naturally from the strong SOC.

To study the generic spin model, we first carry out the semiclassical analysis of the generic spin Hamiltonian in Sec. III. Using the combined Luttinger-Tisza method and classical Monte Carlo simulation, we first determine the classical ground-state phase diagram of the model. We find that the anisotropic $J_{\pm\pm}$ and $J_{z\pm}$ interactions compete with the XXZ part of the model and drive the system into two distinct stripe-ordered phases. Then we implement the classical Monte Carlo simulation to uncover the classical magnetic orders at low temperatures. The ordering temperatures of different phases are determined as well. We find that the ordering temperatures are strongly suppressed near the phase boundary between different ordered phases, suggesting the strong frustration in these regions.

The existing experiments in $YbMgGaO_4$ suggest a disordered quantum ground state. Our generic spin model is expected to describe the interaction between Yb^{3+} local moments. Therefore, it is of importance to understand whether the generic model may support a disordered ground state in the quantum regime, and in which parameter regime such a disordered ground state may exist. For this purpose, in Sec. IV we study the quantum fluctuation through a self-consistent Dyson-Maleev spin-wave analysis and find that the quantum fluctuation is very strong and could melt the magnetic order in the parameter regimes near the phase boundary. We thus expect these regions may turn into a disordered ground state when the quantum nature of the spins is considered.

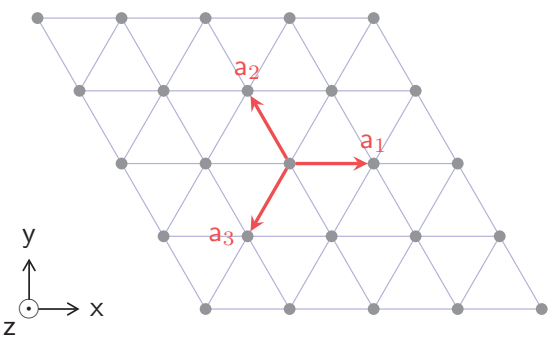

FIG. 1. Triangular lattice and the three nearest neighbors. The inset defines the coordinate system for the spin components.

Since the generic spin model applies broadly to any other triangular system with Kramers' doublet and the long-range order should survive deep inside the ordered regions even for the quantum spins, these magnetic orders should be relevant for other triangular lattice magnets with strong SOC, such as the RCd_3P_3, RZn_3P_3, RCd_3As_3, RZn_3As_3 family, where R is a rare-earth element. It is likely that the magnetic order may appear in some of these materials. In Sec. V, we compute the spin-wave excitation in different ordered phases. Moreover, because the energy scale of the exchange coupling for the rare-earth triangular magnets is usually very small, it is ready to apply strong magnetic fields to fully polarize the spin moments. This allows a direct comparison between the theoretical results and the inelastic neutron scattering measurements in the future experiments both in $YbMgGaO_4$ and other relevant materials.

The remainder of the paper is organized as follows. In Sec. II, we explain the symmetry operation on the spin-orbit-entangled local moments and derive the generic spin model for the rare-earth triangular systems. In Sec. III, we carry out both Luttinger-Tisza analysis and classical Monte Carlo simulation and determine the classical phase diagram. In Sec. IV, we implement the self-consistent Dyson-Maleev spin wave calculation to study the quantum fluctuation in different ordered phase. In Sec. V, we compute the spin-wave excitation in the presence and absence of magnetic fields. Finally, in Sec. VI, we discuss the connection with the experiments and future theoretical directions.

II. THE GENERIC SPIN HAMILTONIAN FOR KRAMERS' DOUBLET

We start with the symmetry transformation properties of the Kramers' doublet. While the discussion in this section is about the Yb^{3+} ion in $YbMgGaO_4$, the symmetry analysis applies generally to any other Kramers' doublet that shares the same symmetry properties on the triangular lattice.

The Yb^{3+} ion contains 13 $4f$ electrons. According to the Hund's rule, we should have the total spin $s = 1/2$ and

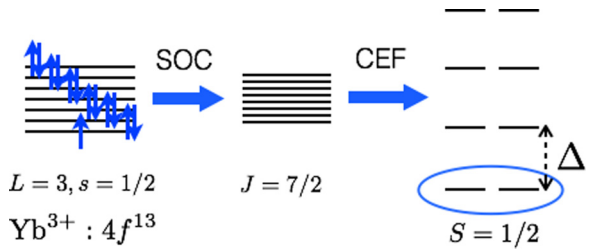

FIG. 2. The formation of the local ground-state Kramers' doublet under the combination of spin-orbit coupling (SOC) and the crystal electric field (CEF). Please refer the text for the detailed description.

the orbital angular momentum $L = 3$ for the Yb^{3+} ion. The 14-fold spin and orbital degeneracy is lifted when the atomic SOC and the crystal electric field are considered. For the $4f$ electrons, the atomic SOC should be considered before the crystal electric field. As we show in Fig. 2, the atomic SOC entangles the orbital angular momentum and the total spin, leading to a total angular momentum $J = 7/2$ with eightfold degeneracy. Just like the Yb^{3+} ion for the pyrochlore ice material $Yb_2Ti_2O_7$ [17], the crystal electric field of the D_{3d} point group further splits the eight $J = 7/2$ states into four pairs of Kramers' doublets. The ground-state doublet is well separated from other excited doublets with an energy gap $\Delta \sim 420$ K and thus can be treated as an effective spin-1/2 degree of freedom at the temperature that is much lower than the energy gap [4,17]. We introduce an effective spin-1/2 local moment, $\mathbf{S}_i$, that operates on the local ground state Kramers' doublet. This effective spin-1/2 degree of freedom for the Yb^{3+} ion is well supported by the low-temperature magnetic entropy that is measured to be $R \ln 2$ per spin [3,4].

This effective spin, $\mathbf{S}$, results from the spin-orbit entanglement of the Yb^{3+} $4f$ electrons. As a consequence, both the position and the orientation of the spins are transformed together under the space-group symmetry operation, and the transformation is given as

$$\mathbf{S}_\mathbf{r} \to \mathrm{Det}[\hat{O}] \cdot \hat{O}^{-1} \cdot \mathbf{S}_{\hat{O}\cdot\mathbf{r}+\mathbf{t}}, \tag{2}$$

where $\hat{O}$ and $\mathbf{t}$ are the matrix and the vector that specify the rotation part and the translation part of the space-group operation, respectively. In contrast, in a magnetic system whose local moment is purely given by the total spin, the spin rotational symmetry would be decoupled from the space-group symmetry operation. The latter merely acts on the positions of the spin moments and does not rotate the spin components. This is the key difference between the strong spin-orbit coupled Mott insulators and a conventional Mott insulator with quenched orbital degrees of freedom.

In $YbMgGaO_4$, the Yb^{3+} ions form a perfect triangular lattice. The interlayer separation between nearby Yb triangular layers is 8.4 Å and is much larger than the intralayer Yb lattice constant that is 3.4 Å [3]. Because the Yb $4f$ electron is very localized spatially, one can safely neglect the interlayer coupling and focus on the intralayer coupling between the Yb local moments. We thus keep the symmetry operation of the space group within each triangular layer. As we show in Fig. 3, the $R\bar{3}m$ space group of $YbMgGaO_4$ contains two translations, T_1 and T_2, along the two crystallographic axes,

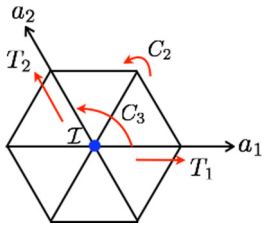

FIG. 3. The space group symmetry operation for the Yb triangular layer.

the threefold rotation, C_3, around the z direction, the twofold rotation, C_2 around the diagonal direction, and an inversion, $\mathcal{I}$, about the triangular lattice site. With these symmetries and their transformations on the spin operators, it is ready to obtain the generic spin Hamiltonian in Eq. (1) that describes the interaction between the local moments.

III. SEMICLASSICAL ANALYSIS: LUTTINGER-TISZA METHOD AND CLASSICAL MONTE CARLO SIMULATION

To obtain the first understanding of the ground-state properties of the generic spin model, in this section we will implement the standard Luttinger-Tisza method and classical Monte Carlo simulation to uncover the magnetic-ordered ground states and to obtain the classical ground-state phase diagram.

A. Luttinger-Tisza method

Here we treat the effective spin $\mathbf{S}_i$ as a classical vector that satisfies the hard-spin constraint $|\mathbf{S}_i| = 1/2$. Following Luttinger and Tisza [18], we first replace the hard-spin constraint with a global constraint, such that

$$\sum_i |\mathbf{S}_i|^2 = \frac{N}{4}, \tag{3}$$

where N is the total number of spins. The classical spin Hamiltonian is then minimized under this global constraint. If the energy minimum turns out to satisfy the local hard-spin constraint as well, then this energy minimum is the true classical ground state.

There are four parameters, J_{zz}, $J_\pm$, $J_{\pm\pm}$, $J_{z\pm}$, in the generic spin model. We first consider the parameter regime when the anisotropic interaction vanishes with $J_{\pm\pm} = 0$ and $J_{z\pm} = 0$. In this regime the spin model reduces to the XXZ model. From the Curie-Weiss temperature results on single crystal $YbMgGaO_4$ samples [3], one finds that both J_{zz} and $J_\pm$ are antiferromagnetic and $J_\pm/J_{zz} \approx 0.915$, which is fixed to this value throughout the paper. The ground state of this XXZ model is simply the well-known 120 ° ordered state with the spins orienting in the xy plane. The ordering wave vector of the 120° state is at

$$\mathbf{k}_c = \left(\frac{4\pi}{3}, 0\right), \tag{4}$$

or its symmetry equivalent wave vectors.

Now we discuss the effect of the anisotropic spin interactions. With a small $|J_{\pm\pm}|$, the minimum of the classical

Hamiltonian under the global constraint slightly deviates from the 120° state and occurs at incommensurate wave vectors. In strong spin-orbit coupled insulators, however, the incommensurate ordering is generically not favored. Because of the intrinsic spin anisotropy that originates from the strong spin-orbit coupling [19], to optimize the spin anisotropy, the ordered spin moments cannot orient freely like the case for an incommensurate state. As a result, we generically have the commensurate spin orders in the strong spin-orbit coupled insulators. Apart from the general understanding, we here provide more specific reasons. Due to the low symmetry of the spin Hamiltonian, the eigenstate that corresponds to the minimum is generically unique, hence one cannot find two orthogonal eigenvectors to construct an incommensurate spiral state that satisfies the hard-spin constraint on every lattice site. Therefore, the incommensurate state cannot be a true classical ground state, and we tentatively regard the 120° state as the candidate classical ground state in the regime with a small $J_{\pm\pm}$.

With a large $|J_{\pm\pm}|$ and/or a large $|J_{z\pm}|$, the minimum of the classical spin Hamiltonian occurs at

$$\mathbf{k}_s = \left(0, \frac{2\pi}{\sqrt{3}}\right), \tag{5}$$

or its symmetry-equivalent wave vectors. Remarkably, this minimum state satisfies the hard-spin constraint and is thus a true ground state. The spin configuration with this ordering wave vector has a stripe order, i.e., the spins order ferromagnetically along one lattice direction and antiferromagnetically along the remaining two lattice directions. To obtain the classical phase diagram in Fig. 4(a), we compare the energies of the 120° state and the stripe-ordered phases. In region I of the phase diagram, the 120° state is obtained. In regions II and III, we find two stripe-ordered phases with different spin orientations. Without loss of generality, we fix the ordering wave vector of the stripe phase to be $\mathbf{k}_s = (0, 2\pi/\sqrt{3})$. Due to the locking of the spin orientation and the ordering wave vector, the spin configuration is fixed as well. With this choice of the ordering wave vector, the spins are pointing in the yz plane [20] and x direction in regions II and III, respectively (see Fig. 4).

Here we elucidate the structure of the classical ground-state phase diagram. The magnetic phases for a negative $J_{z\pm}$ can be simply generated from the ones in the positive $J_{z\pm}$ case by a 180° rotation around the z axis in the spin space. Under this spin rotation,

$$S_i^z \to S_i^z, \tag{6}$$

$$S_i^\pm \to -S_i^\pm, \tag{7}$$

the coupling $J_{z\pm} \to -J_{z\pm}$, while other couplings stay invariant [21]. Therefore, we only consider the phase diagram with a positive $J_{z\pm}$ in Fig. 4(a). In addition, on the horizontal axis with $J_{z\pm} = 0$, the magnetic phases are symmetric about the origin. This is seen by rotating the spins around the z axis by 90°. It transforms the spins as

$$S_i^z \to S_i^z, \tag{8}$$

$$S_i^\pm \to \pm i S_i^\pm, \tag{9}$$

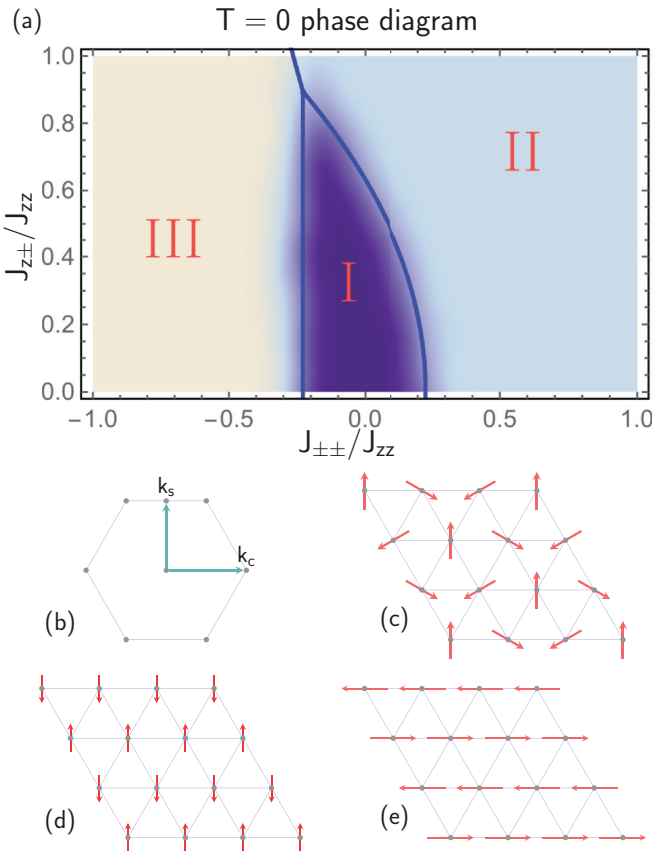

FIG. 4. (a) The classical phase diagram in the zero temperature limit. The solid phase boundaries are determined by the Luttinger-Tisza method, and the colored regions are determined by classical Monte Carlo simulation. (b) Ordering wave vectors $\mathbf{k}_c$ and $\mathbf{k}_s$ drawn in the first Brillouin zone (the hexagon) for the three phases. (c) The 120° order in region I with spins pointing in the xy plane. (d) The stripe order in region II with spins pointing in the yz plane. (e) The stripe order in region III with spins pointing along the x direction.

and the coupling as $J_{\pm\pm} \to -J_{\pm\pm}$. The above properties of the classical phase diagram hold even for the quantum case.

B. Classical Monte Carlo simulation

To further investigate the structure of the classical phase diagram and to extract finite-temperature magnetic properties, we implement the classical Monte Carlo simulation of the classical spin Hamiltonian [22,23]. As we previously explained, the system prefers the commensurate spin orders. So one does not need a large system size to carry out the classical Monte Carlo simulation. The simulation is performed on 6×6 and 12×12 triangular systems. It starts with a randomly chosen initial spin configuration, followed by 5000 transient Monte Carlo steps (MCS) for the system to equilibrate. Within each step, the Metropolis algorithm [24,25] is implemented for sampling, and a method proposed in Ref. [26] is used for updating the spin configurations in the canonical ensemble. The observables are averaged within a sample of size MCS = 50 000.

Since the 120° state (the stripe-ordered phase) has an ordering wave vector $\mathbf{k}_c$ ($\mathbf{k}_s$), we evaluate the spin-spin

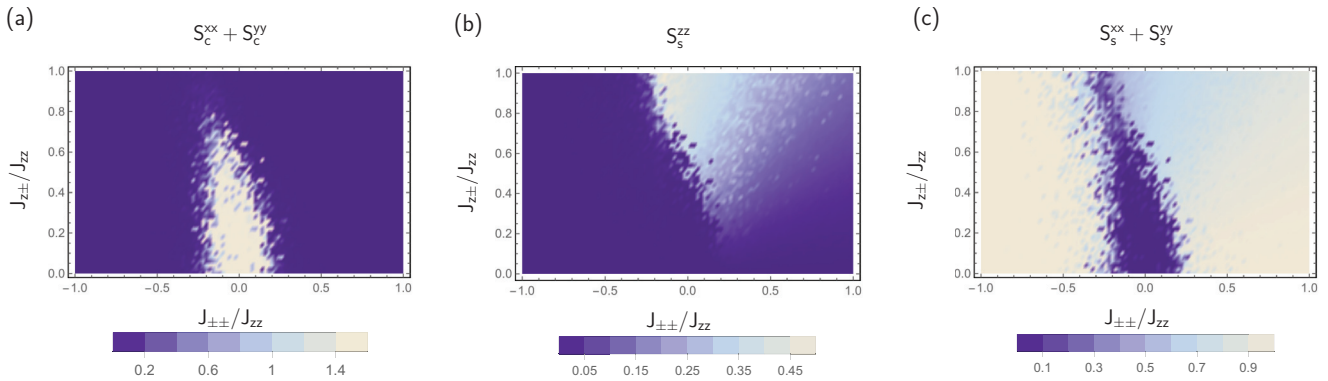

FIG. 5. Spin-spin correlation functions $S_{c/s}^{\alpha\beta}$ at zero temperature are displayed. (a) $S_c^{xx} + S_c^{yy}$ at $T \to 0$. The region with large S_c suggests the 120° order of spins. (b) A finite z-z correlation for the stripe phase helps us distinguish two stripe phases (Fig. 4) due to different signs of $J_{\pm\pm}$. (c) x-x plus y-y correlation for the stripe phase.

correlation functions at the corresponding wave vectors,

$$S_{c/s}^{\alpha\beta} = \frac{1}{N^2} \sum_{i,j} \langle S_i^\alpha S_j^\beta \rangle e^{i\mathbf{k}_{c/s}\cdot(\mathbf{r}_j - \mathbf{r}_i)}, \tag{10}$$

where $\alpha, \beta = x, y, z$. The result is summarized in Fig. 5. In the zero temperature limit, we observe a significant stripe order that signifies the stripe phases away from the central region of the phase diagram. We also notice that as both $J_{\pm\pm}$ and $J_{z\pm}$ increase on the positive side, the spins develop a finite component in the yz plane, distinguishing it from the stripe order with spins pointing along x direction in the negative $J_{\pm\pm}$ region (see Fig. 4).

Near the phase boundaries, not only the neighboring ordered phases are very close in energies, but a large number of classical spin configurations have rather close energies. As a result, thermal fluctuations can easily populate the low-energy spin configurations, even at a temperature much smaller than $|\Theta_{\mathrm{CW}}|$, such that the system may not favor any obvious magnetic order. Therefore, we expect the ordering temperature to be strongly suppressed in these frustrated regions.

The classical Monte Carlo simulation allows us to access the finite-temperature magnetic properties. We can still perform the calculation of the spin correlation function as the temperature is raised from zero. At zero temperature, the system is frozen at its ground state, therefore the deviation of a physical observable $\hat{O}$ (chosen to be $S^{\alpha\beta}$ in this case), $\langle \hat{O}^2 \rangle - \langle \hat{O} \rangle^2$, vanishes. However, at finite temperatures, due to the possibility for spins to flip to another configuration with similar energy, $\hat{O}$ can develop a nonzero deviation. Therefore, the Binder ratios [27,28], defined for the spin-spin correlation functions,

$$r^{\alpha\alpha} = \frac{\langle (S_{c/s}^{\alpha\alpha})^2 \rangle}{\langle S_{c/s}^{\alpha\alpha} \rangle^2}, \tag{11}$$

should attain the value 1 at zero temperature and saturate to a larger value in the high temperature limit. The Binder ratios are scale-independent quantities at the critical temperature T_c, hence T_c can be estimated by finding the crossing of $r^{\alpha\alpha}$-T curves for different lattice sizes. The thermal transition is found to be continuous and no other thermal phases are found in our numerical study of finite-size systems. The result of our simulation is summarized in Fig. 6.

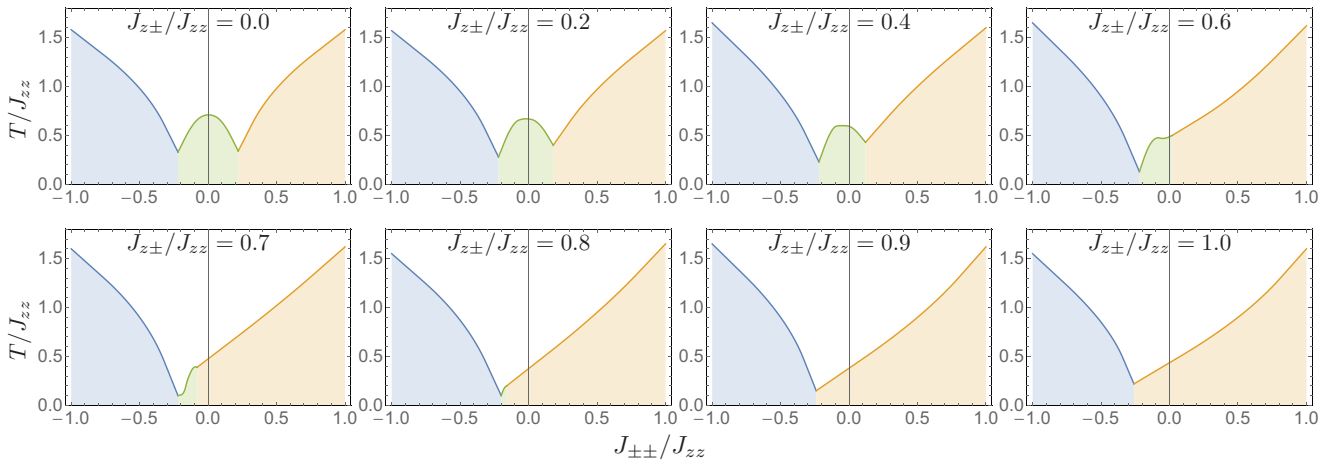

FIG. 6. Cuts through constant $J_{z\pm}$ lines of the three-dimensional finite-temperature phase diagram in the main text. The white region is the high-temperature paramagnetic phase. The solid line indicates the transition temperatures.

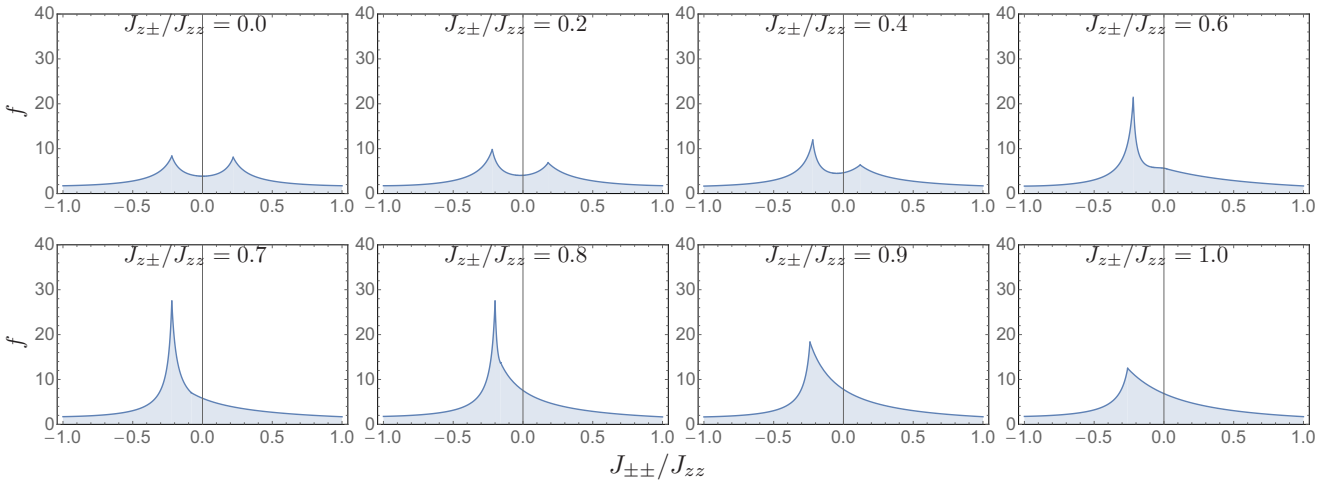

FIG. 7. The frustration parameter $f \equiv |\Theta_{\rm CW}|/T_{\rm N}$ of the corresponding plots in Fig. 6.

It is found that in the parameter regimes near the phase boundary the magnetic ordering temperature is in fact strongly suppressed compared to the Curie-Weiss temperature $|\Theta_{\rm CW}|$. The local moments do not order down to very low temperatures, which indicates the strong spin frustration in these regions. In Fig. 7, we evaluate the frustration parameter,

$$f \equiv \frac{|\Theta_{\rm CW}|}{T_c}, \tag{12}$$

which is an empirical measure of the frustration [29]. Because of the spin anisotropy, the Curie-Weiss temperature depends on the direction of the external magnetic field. To be specific, we choose the Curie-Weiss temperature to be the one when the external field is applied in the xy plane, so we have $\Theta_{\rm CW} = -3J_{\pm}$ [3]. Indeed, the frustration parameter is as large as 20 near the phase boundaries between two neighboring phases (see Fig. 7).

IV. QUANTUM FLUCTUATION AND SELF-CONSISTENT DYSON-MALEEV SPIN-WAVE THEORY

The semiclassical analysis in the previous section gives the classical ground-state phase diagram. When the ground state does support magnetic ordering, the semiclassical treatment does provide a qualitative understanding of the magnetic phases. In this section, we go beyond the semiclassics and access the quantum mechanical nature of the local moments. By considering the quantum fluctuation in the magnetic-ordered phases, we try to understand the stability of the magnetic order in the presence of quantum fluctuations and find out where the disordered state may occur in the phase diagram.

Deep inside each ordered phase, the magnetic order is clearly very robust, and we expect that the quantum fluctuation would merely renormalize the magnetic order. In contrast, near the phase boundary, many classical spin configurations have rather close energies and may strongly enhance the quantum fluctuations. To demonstrate this explicitly, we apply the Dyson-Maleev transformation for the spin operators and solve for the quantum correction to the magnetic order within a self-consistent spin-wave theory [30,31]. To be specific, we focus the analysis on the stripe-ordered phase in region III, and the spin-wave theory in other ordered regions can be obtained likewise. As we show in Sec. III, the spins in region III orient in the $\pm\hat{x}$ directions. We introduce the Dyson-Maleev representation for the spin operators [30,31]:

$$\mathbf{S}_i \cdot \hat{m}_i = S - a_i^\dagger a_i, \tag{13}$$

$$\mathbf{S}_i \cdot [\hat{m}_i \times \hat{z}] = \tfrac{1}{2}[a_i^\dagger (2S - a_i^\dagger a_i) + a_i], \tag{14}$$

$$\mathbf{S}_i \cdot \hat{z} = \frac{1}{2i}[a_i^\dagger (2S - a_i^\dagger a_i) - a_i], \tag{15}$$

where the spin magnitude $S = 1/2$, $\hat{m}_i$ is the direction of the classical spin order and orients along $\hat{x}$ or $-\hat{x}$. Because the stripe-ordered state has two magnetic sublattices, there are two flavors of Dyson-Maleev bosons that describe the magnetic excitation and quantum fluctuation in region III.

In the usual linear spin-wave approximation, one neglects the cubic boson terms in the Dyson-Maleev transformation by setting

$$\mathbf{S}_i \cdot \hat{m}_i = S - a_i^\dagger a_i, \tag{16}$$

$$\mathbf{S}_i \cdot [\hat{m}_i \times \hat{z}] \approx (a_i^\dagger + a_i)/2 \tag{17}$$

$$\mathbf{S}_i \cdot \hat{z} \approx (a_i^\dagger - a_i)/(2i). \tag{18}$$

This approximation is valid when $\langle a_i^\dagger a_i \rangle \ll S$. We substitute the spin operators with the Dyson-Maleev bosons, keep the quadratic part of the spin-wave Hamiltonian, and diagonalize it with the standard Bogoliubov transformation. We proceed to evaluate the quantum correction $\delta m_i \equiv \langle a_i^\dagger a_i \rangle$ and find that δm_i is comparable to the spin magnitude in the parameter regime near the phase boundary. Clearly, the strong quantum fluctuation in these regions invalidates the assumption of the linear spin-wave theory that neglects the boson interaction in the formalism.

To fix the drawbacks of the linear spin-wave approximation, we implement a self-consistent spin-wave calculation in the following. The Dyson-Maleev transformation in Eqs. (13)–(15) has proven to be convenient for studying spin-wave

interaction [32]. With the Dyson-Maleev transformation for the spin operators, we obtain the spin-wave Hamiltonian. In this Hamiltonian, there exist cubic, quartic, quintic, and sextic terms in terms of the Dyson-Maleev bosons. To reduce the spin-wave Hamiltonian down to the quadratic level, we make the mean-field decoupling of the quartic and sextic terms. The quartic and sextic terms are decoupled into various onsite and intersite boson bilinears,

$$\begin{aligned} a_i^\dagger a_i a_j^\dagger a_j \to\ & [a_i^\dagger a_i - \langle a_i^\dagger a_i\rangle]\langle a_j^\dagger a_j\rangle + \langle a_i^\dagger a_i\rangle[a_j^\dagger a_j - \langle a_j^\dagger a_j\rangle] + \langle a_i^\dagger a_j^\dagger\rangle[a_i a_j - \langle a_i a_j\rangle] + [a_i^\dagger a_j^\dagger - \langle a_i^\dagger a_j^\dagger\rangle]\langle a_i a_j\rangle \\ & + \langle a_i^\dagger a_j\rangle[a_j^\dagger a_i - \langle a_j^\dagger a_i\rangle] + [a_i^\dagger a_j - \langle a_i^\dagger a_j\rangle]\langle a_j^\dagger a_i\rangle + \langle a_i^\dagger a_i\rangle\langle a_j^\dagger a_j\rangle + \langle a_i^\dagger a_j^\dagger\rangle\langle a_i a_j\rangle + \langle a_i^\dagger a_j\rangle\langle a_j^\dagger a_i\rangle, \end{aligned} \tag{19}$$

$$\begin{aligned} a_i^\dagger a_j^\dagger a_j^\dagger a_j \to\ & [a_j^\dagger a_j^\dagger - \langle a_j^\dagger a_j^\dagger\rangle]\langle a_i^\dagger a_j\rangle + a_j^\dagger a_j^\dagger[a_i^\dagger a_j - \langle a_i^\dagger a_j\rangle] + 2[a_j^\dagger a_j - \langle a_j^\dagger a_j\rangle]\langle a_i^\dagger a_j^\dagger\rangle + 2\langle a_j^\dagger a_j\rangle[a_i^\dagger a_j^\dagger - \langle a_i^\dagger a_j^\dagger\rangle] \\ & + \langle a_j^\dagger a_j^\dagger\rangle\langle a_i^\dagger a_j\rangle + 2\langle a_j^\dagger a_j\rangle\langle a_i^\dagger a_j^\dagger\rangle, \end{aligned} \tag{20}$$

$$\begin{aligned} a_i^\dagger a_i^\dagger a_i a_j^\dagger a_j^\dagger a_j \to\ & [a_i^\dagger a_i^\dagger - \langle a_i^\dagger a_i^\dagger\rangle]\langle a_i a_j^\dagger a_j^\dagger a_j\rangle + 2[a_i^\dagger a_i - \langle a_i^\dagger a_i\rangle]\langle a_i^\dagger a_j^\dagger a_j^\dagger a_j\rangle + [a_j^\dagger a_j^\dagger - \langle a_j^\dagger a_j^\dagger\rangle]\langle a_i^\dagger a_i^\dagger a_i a_j\rangle \\ & + 2[a_j^\dagger a_j - \langle a_j^\dagger a_j\rangle]\langle a_i^\dagger a_i^\dagger a_i a_j^\dagger\rangle + 4[a_i^\dagger a_j^\dagger - \langle a_i^\dagger a_j^\dagger\rangle]\langle a_i^\dagger a_i a_j^\dagger a_j\rangle + 2[a_i^\dagger a_j - \langle a_i^\dagger a_j\rangle]\langle a_i^\dagger a_i a_j^\dagger a_j^\dagger\rangle \\ & + 2[a_i a_j^\dagger - \langle a_i a_j^\dagger\rangle]\langle a_i^\dagger a_i^\dagger a_j^\dagger a_j\rangle + [a_i a_j - \langle a_i a_j\rangle]\langle a_i^\dagger a_i^\dagger a_j^\dagger a_j^\dagger\rangle + \langle a_i^\dagger a_i^\dagger a_i a_j^\dagger a_j^\dagger a_j\rangle, \end{aligned} \tag{21}$$

where the expectation "$\langle\cdots\rangle$" is evaluated with respect to the ground state of the quadratic spin-wave Hamiltonian that is defined later, and we have

$$\begin{aligned} \langle a_i^\dagger a_i^\dagger a_i a_j^\dagger a_j^\dagger a_j\rangle =\ & 2\langle a_i^\dagger a_i^\dagger\rangle\langle a_i a_j^\dagger\rangle\langle a_j^\dagger a_j\rangle + \langle a_i^\dagger a_i^\dagger\rangle\langle a_j^\dagger a_j^\dagger\rangle\langle a_i a_j\rangle + 4\langle a_i^\dagger a_i\rangle\langle a_j^\dagger a_j\rangle\langle a_i^\dagger a_j^\dagger\rangle \\ & + 2\langle a_i^\dagger a_i\rangle\langle a_j^\dagger a_j^\dagger\rangle\langle a_i^\dagger a_j\rangle + 4\langle a_i^\dagger a_j^\dagger\rangle\langle a_i^\dagger a_j\rangle\langle a_i a_j^\dagger\rangle + 2\langle a_i^\dagger a_j^\dagger\rangle\langle a_i^\dagger a_j^\dagger\rangle\langle a_i a_j\rangle, \end{aligned} \tag{22}$$

and

$$\langle a_i a_j^\dagger a_j^\dagger a_j\rangle = 2\langle a_i a_j^\dagger\rangle\langle a_j^\dagger a_j\rangle + \langle a_i a_j\rangle\langle a_j^\dagger a_j^\dagger\rangle, \tag{23}$$

$$\langle a_i^\dagger a_j^\dagger a_j^\dagger a_j\rangle = 2\langle a_i^\dagger a_j^\dagger\rangle\langle a_j^\dagger a_j\rangle + \langle a_i^\dagger a_j\rangle\langle a_j^\dagger a_j^\dagger\rangle, \tag{24}$$

$$\langle a_i^\dagger a_i^\dagger a_i a_j\rangle = 2\langle a_i^\dagger a_i\rangle\langle a_i^\dagger a_j\rangle + \langle a_i^\dagger a_i^\dagger\rangle\langle a_i a_j\rangle, \tag{25}$$

$$\langle a_i^\dagger a_i^\dagger a_i a_j^\dagger\rangle = 2\langle a_i^\dagger a_i\rangle\langle a_i^\dagger a_j^\dagger\rangle + \langle a_i^\dagger a_i^\dagger\rangle\langle a_i a_j^\dagger\rangle, \tag{26}$$

$$\langle a_i^\dagger a_i a_j^\dagger a_j\rangle = \langle a_i^\dagger a_i\rangle\langle a_j^\dagger a_j\rangle + \langle a_i^\dagger a_j^\dagger\rangle\langle a_i a_j\rangle + \langle a_i^\dagger a_j\rangle\langle a_j^\dagger a_i\rangle, \tag{27}$$

$$\langle a_i^\dagger a_i a_j^\dagger a_j^\dagger\rangle = \langle a_i^\dagger a_i\rangle\langle a_j^\dagger a_j^\dagger\rangle + 2\langle a_i^\dagger a_j^\dagger\rangle\langle a_i a_j^\dagger\rangle, \tag{28}$$

$$\langle a_i^\dagger a_i^\dagger a_j^\dagger a_j\rangle = 2\langle a_i^\dagger a_j^\dagger\rangle\langle a_i^\dagger a_j\rangle + \langle a_i^\dagger a_i^\dagger\rangle\langle a_j^\dagger a_j\rangle, \tag{29}$$

$$\langle a_i^\dagger a_i^\dagger a_j^\dagger a_j^\dagger\rangle = 2\langle a_i^\dagger a_j^\dagger\rangle\langle a_i^\dagger a_j^\dagger\rangle + \langle a_i^\dagger a_i^\dagger\rangle\langle a_j^\dagger a_j^\dagger\rangle. \tag{30}$$

The decoupling of the cubic and quintic terms leads to linear terms in the Dyson-Maleev bosons that should all cancel out by the stability requirement of the classical ground state. Therefore, the decoupling of the cubic and quintic terms does not introduce extra quadratic terms into the spin-wave Hamiltonian.

After defining the Fourier transform of the Dyson-Maleev boson operators, the quadratic spin-wave Hamiltonian can be organized as

$$H_{\rm sw} = \sum_{\mathbf{k}\in \mathrm{BZ}'} (A_{\mathbf{k}}^\dagger, A_{-\mathbf{k}}) \begin{pmatrix} F_{\mathbf{k}} & G_{\mathbf{k}}^\dagger \\ G_{\mathbf{k}} & F_{-\mathbf{k}} \end{pmatrix} \begin{pmatrix} A_{\mathbf{k}} \\ A_{-\mathbf{k}}^\dagger \end{pmatrix}, \tag{31}$$

where $A_{\mathbf{k}} = (a_{1\mathbf{k}}, a_{2\mathbf{k}})$ is the vector of the Dyson-Maleev boson annihilation operator, the subindices "1" and "2" label the two sublattices of the magnetic unit cell, and BZ′ is the magnetic Brioullin zone of the stripe-ordered phase. $F_{\mathbf{k}}$ and $G_{\mathbf{k}}$ are 2×2 matrices and depend on the mean-field parameters that were introduced as boson bilinears. The quadratic spin-wave Hamiltonian is diagonalized by the standard Bogoliubov transformation $Q_{\mathbf{k}}$ [33],

$$\begin{pmatrix} B_{\mathbf{k}} \\ B_{-\mathbf{k}}^\dagger \end{pmatrix} = Q_{\mathbf{k}} \begin{pmatrix} A_{\mathbf{k}} \\ A_{-\mathbf{k}}^\dagger \end{pmatrix}, \tag{32}$$

where $B_{\mathbf{k}} = (b_{1\mathbf{k}}, b_{2\mathbf{k}})$ refers to the set of Bogoliubov bosons, and $Q_{\mathbf{k}}$ is a 4×4 matrix that defines the Bogoliubov transformation. From the ground state of the quadratic spin wave Hamiltonian, we evaluate the mean-field boson bilinears ($\langle a_i^\dagger a_i\rangle$, $\langle a_i^\dagger a_j\rangle$, $\langle a_i^\dagger a_i^\dagger\rangle$, and $\langle a_i^\dagger a_j^\dagger\rangle$). As the spin-wave Hamiltonian depends on these boson bilinears, so we solve for them self-consistently by an iteration method.

The quantum correction to the magnetic order is evaluated by

$$\begin{aligned} \delta m = \langle a_i^\dagger a_i\rangle &= \frac{1}{N}\sum_i \langle a_i^\dagger a_i\rangle \\ &= \frac{1}{2}\left\{\frac{1}{N}\sum_{\mathbf{k}}\sum_{i=1}^{2}[Q_{\mathbf{k}}^\dagger Q_{\mathbf{k}}]_{ii} - 1\right\}, \end{aligned} \tag{33}$$

where N is the number of lattice sites and we have used the simple fact that the state in region III is invariant under the combined operation of time reversal and the translation T_2. If $\delta m > S$, the quantum fluctuation is very strong and completely melts the magnetic order. As we show in Fig. 8, the quantum fluctuation is indeed quite strong and melts the magnetic order in the regions near the phase boundary. This suggests the ground state is likely to be disordered in these regions.

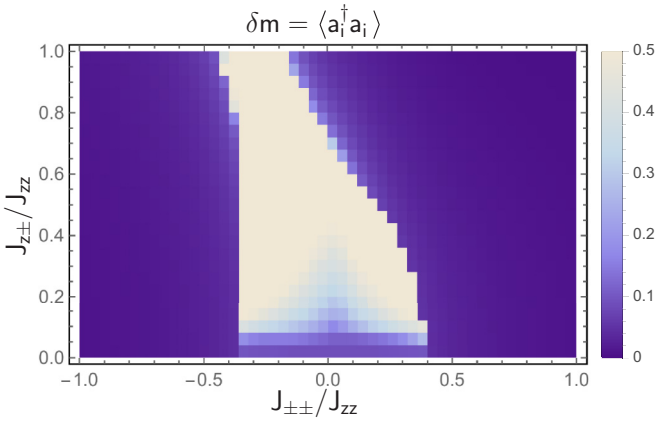

FIG. 8. Quantum correction (δm) to the magnetic orders that is calculated within the self-consistent spin-wave theory on a 80×80 lattice. The region near phase boundary where δm exceeds the spin magnitude with $\delta m \geqslant 1/2$ is marked in beige.

V. MAGNETIC EXCITATIONS WITH AND WITHOUT EXTERNAL MAGNETIC FIELDS

In this section, we study the properties of the magnetic excitations in different ordered phases as well as in the presence of strong magnetic fields.

A. Linear spin-wave theory for the three ordered phases

Since the quantum fluctuation is found to be very weak deep inside each ordered phases, it is legitimate to apply the linear spin-wave theory to study the magnetic excitation in the strongly ordered regimes. In Fig. 9, we plot the representative spin-wave dispersions for the three ordered phases. Due to the anisotropic spin interaction, the system does not have any continuous symmetry, so generically the spin-wave spectrum is fully gapped. This is indeed the case for the two stripe-ordered phases in Figs. 9(a) and 9(b). In Fig. 9(c), the parameters are chosen that the spin model reduces to a XXZ model. Due to the continuous U(1) symmetry breaking, the spin-wave spectrum has one gapless mode. As one moves away from this special point, we expect the spectrum should be gapped.

B. Polarized phases and strong magnetic fields

For the rare-earth magnets, the $4f$ electrons are very localized. As a result, the exchange interaction between the rare-earth local moments are usually very small. For $YbMgGaO_4$, the couplings in the spin Hamiltonian are of the order of 1–4 K. Therefore, an external magnetic field of the order of 10 T is probably sufficient to polarize the local moments. For the magnetic field that is applied along the z direction, we have the spin Hamiltonian,

$$H_Z = H - h_z \sum_i S_i^z. \tag{34}$$

Here $h_z \equiv g_z \mu_B B_z$ and the g_z is the Landé factor for magnetic field in z direction. When the field h_z is strong enough, the spin is polarized along z. To obtain the magnetic excitation of this polarized state, we use the linear spin-wave theory and

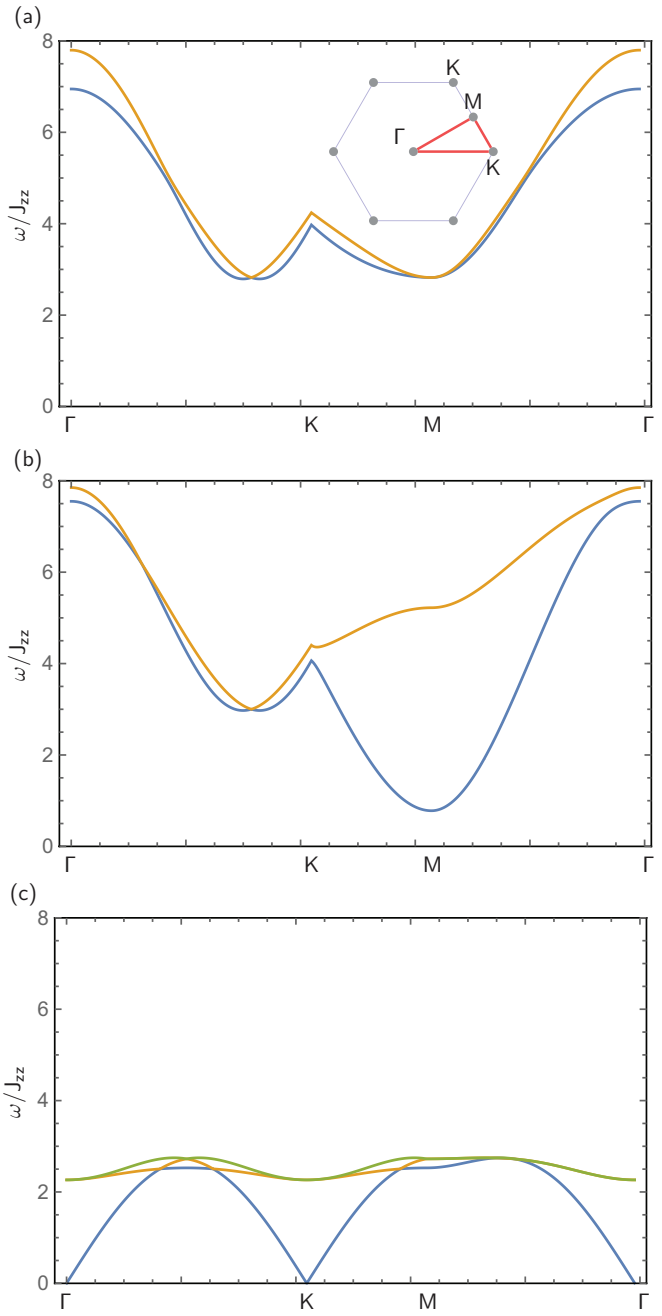

FIG. 9. Spin-wave dispersion along high symmetry momentum points. (a) Spin-wave dispersion in x-stripe phase, at $J_{\pm\pm} = -0.9J_{zz}$, $J_{z\pm} = 0.1J_{zz}$. Inset: The first Brillouin zone, with red loop of high-symmetry points along which we plot the dispersion indicated. (b) Spin-wave dispersion in yz-stripe phase, at $J_{\pm\pm} = 0.8J_{zz}$, $J_{z\pm} = 0.8J_{zz}$. (c) Spin-wave dispersion in 120° phase, at $J_{\pm\pm} = J_{z\pm} = 0$.

transform the spin operators as

$$S_i^z = \tfrac{1}{2} - c_i^\dagger c_i, \tag{35}$$

$$S_i^+ = c_i, \tag{36}$$

$$S_i^- = c_i^\dagger. \tag{37}$$

We then plug this transformation in the Hamiltonian H_Z and keep the bilinear terms of boson operators. The magnetic

excitation only has one branch and is simply given by

$$\Omega_{\mathrm{Z},\mathbf{k}} = \left\{ \left[h_z - 3J_{zz} + 2J_{\pm} \sum_{i=1}^{3} \cos(\mathbf{k}\cdot\mathbf{a}_i) \right]^2 - 4J_{\pm\pm}^2 | \cos(\mathbf{k}\cdot\mathbf{a}_1) + e^{-i\frac{2\pi}{3}} \cos(\mathbf{k}\cdot\mathbf{a}_2) + e^{i\frac{2\pi}{3}} \cos(\mathbf{k}\cdot\mathbf{a}_3)|^2 \right\}^{1/2}. \quad (38)$$

The $J_{z\pm}$ coupling is absent in the above spin-wave dispersion. This is because the $J_{z\pm}$ interaction does not generate any quadratic term to the spin-wave Hamiltonian.

For the external field in the x direction, we have

$$H_{\mathrm{X}} = H - h_x \sum_i S_i^x, \quad (39)$$

where $h_x \equiv g_x \mu_B B_x$ and g_x is the Landé factor for magnetic field in x direction. Due to the planar geometry of the lattice, we have $g_x \neq g_z$ [3]. In the strong field limit, the local moment is polarized along the x direction, and we transform the spin operators as

$$S_i^x = \tfrac{1}{2} - d_i^\dagger d_i\,, \quad (40)$$

$$S_i^y = \tfrac{1}{2}(d_i + d_i^\dagger), \quad (41)$$

$$S_i^z = \frac{1}{2i}(d_i - d_i^\dagger). \quad (42)$$

Under the linear spin wave approximation, the magnetic excitation is given as

$$\Omega_{\mathrm{X},\mathbf{k}} = \left(\left\{ (h_x - 6J_{\pm}) + \left(J_{\pm} - J_{\pm\pm} + \frac{J_{zz}}{2} \right) \cos(\mathbf{k}\cdot\mathbf{a}_1) + \left(J_{\pm} + \frac{J_{\pm\pm}}{2} + \frac{J_{zz}}{2} \right) [\cos(\mathbf{k}\cdot\mathbf{a}_2) + \cos(\mathbf{k}\cdot\mathbf{a}_3)] \right\}^2 - \left| \left(J_{\pm} - J_{\pm\pm} - \frac{J_{zz}}{2} + iJ_{z\pm} \right) \cos(\mathbf{k}\cdot\mathbf{a}_1) + \left(J_{\pm} + \frac{J_{\pm\pm}}{2} - \frac{J_{zz}}{2} - i\frac{J_{z\pm}}{2} \right) \times [\cos(\mathbf{k}\cdot\mathbf{a}_2) + \cos(\mathbf{k}\cdot\mathbf{a}_3)] \right|^2 \right)^{1/2}, \quad (43)$$

where all the four couplings enter into the dispersion. In Fig. 10, we plot the spin-wave dispersion along high-symmetry momentum points. In practice, it is ready to measure the dynamic spin structure factor in $YbMgGaO_4$ and other rare-earth triangular antiferromagnets to extract the spin-wave dispersion in the strong magnetic fields. By comparing the dispersion with the theoretical prediction, one may fully specify the microscopic spin Hamiltonian and quantitatively determine all the couplings.

VI. DISCUSSION

Our initial treatment of the generic spin model in Sec. III is semiclassical, and the classical ground states that we found are magnetically ordered. Due to the strong spin anisotropy that arises from the strong SOC, the orientation of the local moments is locked with the ordering wave vector in these classical orders. The magnetic excitations in different ordered phases generically have an excitation gap. Again, this is the spin anisotropy that completely breaks all the continuous spin rotational symmetry.

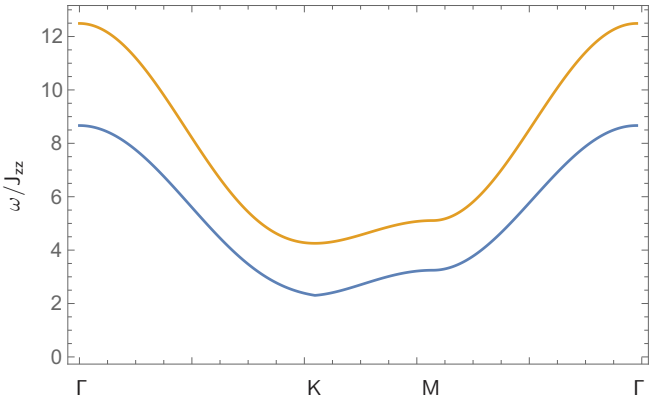

FIG. 10. Spin-wave dispersion when applying external magnetic field along x direction (upper yellow line) and z direction (lower blue line). Here the external field h_z and h_x is taken to be $10J_{zz}$, and anisotropic exchange couplings $J_{z\pm}$ and $J_{\pm\pm}$ are taken to be $0.3J_{zz}$ and $0.2J_{zz}$, respectively.

Our results are quite suggestive for identifying the parameter regime of possible disordered ground states of the generic model for the quantum spins. As we show in Sec. IV, the quantum fluctuation is indeed quite strong in certain parameter regimes and could, in fact, completely destroy the magnetic order. Therefore, if a quantum spin liquid state does appear in the phase diagram of the generic spin model for the triangular lattice, it would most likely occur in these frustrated regions near the phase boundaries between different ordered states.

A. Materials survey

Here we turn to a discussion of relevant materials that have been studied experimentally.

1. $YbMgGaO_4$

The Yb^{3+} local moments in $YbMgGaO_4$ were found to be disordered down to the lowest measurable temperature in the existing experiments. It was suggested to be a U(1) quantum spin liquid with a spinon Fermi surface [34] by one of the author and collaborators [3]. Whether it is a quantum spin liquid or not is not quite clear at this stage. To elucidate the nature of the disordered ground state, an inelastic neutron-scattering measurement at low temperatures is certainly more desirable. On the theoretical side, however, it is more helpful to know precisely the actual parameters in the generic model for $YbMgGaO_4$. The parameters that were determined from the early thermodynamic measurements do overlap significantly with the disordered parameter region in Fig. 8. As we discuss in Sec. V, in the future experiment one could apply strong magnetic fields to polarize the spin and measure the spin-wave dispersion in an inelastic neutron-

scattering measurement. After the disordered parameter region and the actual parameters are determined, the numerical approaches such as variational wave function and density matrix renormalization group may be applied.

2. RZn_3P_3, RCd_3P_3, RZn_3As_3, *and* RCd_3As_3

In the RZn_3P_3, RCd_3P_3, RZn_3As_3, and RCd_3As_3 materials' family, the rare-earth ions, R^{3+}, form triangular layers [5–8]. Since the interlayer separation is much larger than the intralayer lattice constant, one can safely neglect the interlayer coupling. In $CeCd_3P_3$, the intralayer lattice constant is 4.28 Å, while the interlayer distance is 10.5 Å [5]. As we show in Table I, almost all compounds in the RZn_3P_3, RCd_3P_3, RZn_3As_3, and RCd_3As_3 family have the space group $P6_3/mmc$. After we restrict the space-group symmetry of $P6_3/mmc$ to a single triangular layer, the remaining symmetry elements are identical to the ones that are listed for $YbMgGaO_4$ in Sec. II. Therefore, if the rare-earth local moment in this family of materials is the same kind of Kramers' doublet as the Yb^{3+} ion in $YbMgGaO_4$, the local moment interaction is described by the same generic model in Eq. (1). From the crystal electric field analysis in Ref. [5], the ground-state doublet of the Ce^{3+} ion in $CeCd_3P_3$ does belong to the same kind of Kramers' doublet as the Yb^{3+} ion in $YbMgGaO_4$. Because the system remains paramagnetic down to 0.48 K, the authors in Ref. [5] proposed a possible quantum spin-liquid ground state. One may thus wonder whether the possible quantum spin liquid in $CeCd_3P_3$ is in the same phase as the one that was proposed for $YbMgGaO_4$. More experiments such as neutron scattering or NMR measurements on single-crystal samples are certainly needed.

Among this family of materials, $CeZn_3P_3$ is known to develop an antiferromagnetic order at 0.8 K [7]. The precise magnetic-ordering structure is not known from the existing experiments. It is thus of great interest to examine whether the antiferromagnetic order in $CeZn_3P_3$ belongs to one of the orders in our phase diagram.

If the rare-earth ion contains even number of $4f$ electrons like the Pr^{3+} ion in $PrZn_3As_3$, the local ground-state doublet is a non-Kramers' doublet. For such a doublet, the in-plane components, S^x and S^y, of the effective spin are even under time reversal symmetry, while the out-of-plane component, S^z, is odd under time-reversal symmetry. This property immediately forbids the presence of the $J_{z\pm}$ term in Eq. (1) for the local moment interaction. In the simplified model, there are only three parameters: J_{zz}, $J_{\pm}$, and $J_{\pm\pm}$. The analysis of the full phase diagram of the simplified model for non-Kramers' doublets will be left for future work.

Finally, we point out one special Kramers' doublet that was dubbed dipole-octupole Kramers' doublet in Ref. [35]. Dipole-octupole Kramers' doublet occurs when the two ground-state wave functions of the doublet are linear superpositions of states that have J^z equal to odd integer multiples of 3/2. Each ground state corresponds to the one-dimensional irreducible representation of the D_{3d} point group. The twofold Kramers' degeneracy is protected by time reversal symmetry. Dipole-octupole doublet is found to exist in the Nd^{3+} ions of various Nd-based pyrochlore materials and the Ce^{3+} ion of $Ce_2Sn_2O_7$ [35–41]. If the R^{3+} ion in some compounds in the triangular antiferromagnets belongs to dipole-octupole doublet, the local moment interaction would be described by an XYZ-like model. We will discuss the dipole-octupole doublet in a forthcoming work. Nevertheless, the Yb^{3+} ion in $YbMgGaO_4$ and the Ce^{3+} ion in $CeCd_3P_3$ are not dipole-octupole doublets [4,5].

3. $R_2O_2CO_3$

Rare-earth oxycarbonates $R_2O_2CO_3$ (R = Nd, Sm, Dy) is another layered triangular antiferromagnet family that is discovered quite recently. All these materials crystallize in a hexagonal structure with the same space group as $CeCd_3P_3$. Although all three magnetic ions are Kramers' doublet, the crystal-field ground states are not carefully studied in the existing experiments [9]. If these Kramers' doublets are not dipole-octupole doublets, the local moment interaction is given by our anisotropic model in Eq. (1). The precise magnetic ordered structure is unknown, so it is of interest to study the magnetic structure and the magnetic excitation of these systems in the future.

B. Summary

To summarize, we analyzed the generic spin Hamiltonian that describes the interaction between the spin-orbit-entangled Kramers' doublet local moments. We have obtained the magnetic phase diagram that includes three distinct ordered phases. We have further identified the possible disordered region that might host disordered ground states for the Yb local moments in $YbMgGaO_4$ [3]. We carefully studied the magnetic excitation in different ordered phases as well as in the presence of strong magnetic fields. The ordered phases and the magnetic excitations may be detected in future experiments in the strong spin-orbit-coupled triangular antiferromagnets.

As the generic model applies to any other Kramers' doublet with the same symmetry properties, to further justify the applicability of this model, it is thus of great interest to experimentally study the magnetic properties of other rare-earth-based triangular materials and access the magnetic orders in the phase diagram and the magnetic transition from the possible disordered states. Apart from the rare-earth systems, the spin-orbit-entangled Kramers' doublet local moments can appear in the partially filled t_{2g} shells such as triangular lattice iridates [2]. Given the $4d$ or $5d$ nature of the local moments, the exchange interaction is certainly enhanced, and thus one could probe the magnetic properties at a much higher temperature than the rare-earth systems.

ACKNOWLEDGMENTS

We acknowledge Yuesheng Li (Renmin University) and Qingming Zhang (Renmin University) for the previous collaboration, Leon Balents and Patrick Lee for correspondences. We thank Xi Dai, Fengren Fan, Jiangping Hu, Dunghai Lee, Shiyan Li, Yuanming Lu, Yang Qi, Fa Wang, Nanlin Wang, Zhong Wang, Hua Wu, Hong Yao, Rong Yu, Yue Yu, Jize Zhao, Fuchun Zhang, Jun Zhao, and Yi Zhou for valuable conversation. We are particularly indebted to Zhong Wang at the Institute of Advanced Study of Tsinghua University for hosting our stay where part of the work was completed. This work is supported by the start-up fund of Fudan University and the One-Thousand Young Talent Program of China.

[1] M. Z. Hasan and C. L. Kane, Colloquium: Topological insulators, Rev. Mod. Phys. **82**, 3045 (2010).

[2] William Witczak-Krempa, Gang Chen, Yong Baek Kim, and Leon Balents, Correlated quantum phenomena in the strong spin-orbit regime, Annu. Rev. Condens. Matter Phys. **5**, 57 (2014).

[3] Yuesheng Li, Gang Chen, Wei Tong, Li Pi, Juanjuan Liu, Zhaorong Yang, Xiaoqun Wang, and Qingming Zhang, Rare-Earth Triangular Lattice Spin Liquid: A Single-Crystal Study of $YbMgGaO_4$, Phys. Rev. Lett. **115**, 167203 (2015).

[4] Yuesheng Li, Haijun Liao, Zhen Zhang, Shiyan Li, Feng Jin, Langsheng Ling, Lei Zhang, Youming Zou, Li Pi, Zhaorong Yang, Junfeng Wang, Zhonghua Wu, and Qingming Zhang, Gapless quantum spin liquid ground state in the two-dimensional spin-1/2 triangular antiferromagnet $YbMgGaO_4$, Sci. Rep. **5**, 16419 (2015).

[5] S. Higuchi, Y. Noshima, N. Shirakawa, M. Tsubota, and J. Kitagawa, Optical, transport and magnetic properties of new compound $CeCd_3P_3$, Mater. Res. Express **3**, 056101 (2016).

[6] A. T. Nientiedt and W. Jeitschko, The series of rare earth zinc phosphides RZn_3P_3 (R=y, La-Nd, Sm, Gd-Er) and the corresponding cadmium compound $PrCd_3P_3$, J. Solid State Chem. **146**, 483 (1999).

[7] A. Yamada, N. Hara, K. Matsubayashi, K. Munakata, C. Ganguli, A. Ochiai, T. Matsumoto, and Y. Uwatoko, Effect of pressure on the electrical resistivity of $CeZn_3P_3$, J. Phys.: Conf. Ser. **215**, 012031 (2010).

[8] S. S. Stoyko and A. Mar, Ternary rare-earth arsenides $REZn_3As_3$(RE = La-Nd,Sm) and $RECd_3As_3$(RE = La-Pr), Inorg. Chem. **50**, 11152 (2011).

[9] U. Arjun, K. Brinda, M. Padmanabhan, and R. Nath, Magnetic properties of layered rare-earth oxy-carbonates $Ln_2O_2Co_3$ (Ln=Nd, Sm, and Dy), Solid State Commun. **240**, 1 (2016).

[10] Gang Chen and Leon Balents, Spin-orbit effects in $na_4ir_3o_8$: A hyper-kagome lattice antiferromagnet, Phys. Rev. B **78**, 094403 (2008).

[11] Kai Li, Shun-Li Yu, and Jian-Xin Li, Global phase diagram, possible chiral spin liquid, and topological superconductivity in the triangular kitaevheisenberg model, New J. Phys. **17**, 043032 (2015).

[12] Gang Chen, Rodrigo Pereira, and Leon Balents, Exotic phases induced by strong spin-orbit coupling in ordered double perovskites, Phys. Rev. B **82**, 174440 (2010).

[13] S. H. Curnoe, Structural distortion and the spin liquid state in $Tb_2Ti_2O_7$, Phys. Rev. B **78**, 094418 (2008).

[14] Shigeki Onoda and Yoichi Tanaka, Quantum Melting of Spin Ice: Emergent Cooperative Quadrupole and Chirality, Phys. Rev. Lett. **105**, 047201 (2010).

[15] Gang Chen and Leon Balents, Spin-orbit coupling in d^2 ordered double perovskites, Phys. Rev. B **84**, 094420 (2011).

[16] G. Jackeli and G. Khaliullin, Mott Insulators in the Strong Spin-Orbit Coupling Limit: From Heisenberg to a Quantum Compass and Kitaev Models, Phys. Rev. Lett. **102**, 017205 (2009).

[17] Kate A. Ross, Lucile Savary, Bruce D. Gaulin, and Leon Balents, Quantum Excitations in Quantum Spin Ice, Phys. Rev. X **1**, 021002 (2011).

[18] J. M. Luttinger and L. Tisza, Theory of dipole interaction in crystals, Phys. Rev. **70**, 954 (1946).

[19] Hiroaki Ishizuka and Leon Balents, Switching of magnetic anisotropy in a fcc antiferromagnet with direction-dependent interactions, Phys. Rev. B **92**, 020411 (2015).

[20] The actual spin orientation depends on the couplings.

[21] Lucile Savary and Leon Balents, Coulombic Quantum Liquids in Spin-1/2 Pyrochlores, Phys. Rev. Lett. **108**, 037202 (2012).

[22] Hikaru Kawamura and Seiji Miyashita, Phase transition of the two-dimensional Heisenberg antiferromagnet on the triangular lattice, J. Phys. Soc. Jpn. **53**, 4138 (1984).

[23] B.W. Southern and H.-J. Xu, Monte carlo study of the heisenberg antiferromagnet on the triangular lattice, Phys. Rev. B **52**, R3836 (1995).

[24] Nicholas Metropolis, Arianna W. Rosenbluth, Marshall N. Rosenbluth, Augusta H. Teller, and Edward Teller, Equation of state calculations by fast computing machines, J. Chem. Phys. **21**, 1087 (1953).

[25] W. K. Hastings, Monte carlo sampling methods using markov chains and their applications, Biometrika **57**, 97 (1970).

[26] George Marsaglia, Choosing a point from the surface of a sphere, Ann. Math. Statist. **43**, 645 (1972).

[27] K. Binder, Finite size scaling analysis of ising model block distribution functions, Z. Phys. B **43**, 119 (1981).

[28] K Binder, Applications of monte carlo methods to statistical physics, Rep. Prog. Phys. **60**, 487 (1997).

[29] A P Ramirez, Strongly geometrically frustrated magnets, Annu. Rev. Mater. Sci. **24**, 453 (1994).

[30] Freeman J. Dyson, General theory of spin-wave interactions, Phys. Rev. **102**, 1217 (1956).

[31] S. V. Maleev, Sov. Phys. JETP **64**, 654 (1958).

[32] C. M. Canali, S. M. Girvin, and Mats Wallin, Spin-wave velocity renormalization in the two-dimensional heisenberg antiferromagnet at zero temperature, Phys. Rev. B **45**, 10131 (1992).

[33] Adrian Del Maestro and Michel J. P. Gingras, Low-temperature specific heat and possible gap to magnetic excitations in the heisenberg pyrochlore antiferromagnet $Gd_2Sn_2O_7$, Phys. Rev. B **76**, 064418 (2007).

[34] Sung-Sik Lee and Patrick A. Lee, U(1) Gauge Theory of the Hubbard Model: Spin Liquid States and Possible Application to κ-(BEDT-TTF)$_2$Cu$_2$(CN)$_3$, Phys. Rev. Lett. **95**, 036403 (2005).

[35] Yi-Ping Huang, Gang Chen, and Michael Hermele, Quantum Spin Ices and Topological Phases from Dipolar-Octupolar Doublets on the Pyrochlore Lattice, Phys. Rev. Lett. **112**, 167203 (2014).

[36] Romain Sibille, Elsa Lhotel, Vladimir Pomjakushin, Chris Baines, Tom Fennell, and Michel Kenzelmann, Candidate Quantum Spin Liquid in the Ce^{3+} Pyrochlore Stannate $Ce_2Sn_2O_7$, Phys. Rev. Lett. **115**, 097202 (2015).

[37] E. Lhotel, S. Petit, S. Guitteny, O. Florea, M. Ciomaga Hatnean, C. Colin, E. Ressouche, M. R. Lees, and G. Balakrishnan, Fluctuations and All-In–All-Out Ordering in Dipole-Octupole $Nd_2Zr_2O_7$, Phys. Rev. Lett. **115**, 197202 (2015).

[38] A. Bertin, P. Dalmas de Réotier, B. Fåk, C. Marin, A. Yaouanc, A. Forget, D. Sheptyakov, B. Frick, C. Ritter, A. Amato, C. Baines, and P. J. C. King, $Nd_2Sn_2O_7$: An All-in–all-out pyrochlore magnet with no divergence-free field and anomalously slow paramagnetic spin dynamics, Phys. Rev. B **92**, 144423 (2015).

[39] V. K. Anand, A. K. Bera, J. Xu, T. Herrmannsdörfer, C. Ritter, and B. Lake, Observation of long-range magnetic ordering in pyrohafnate $Nd_2Hf_2O_7$: A neutron diffraction study, Phys. Rev. B **92**, 184418 (2015).

[40] J. Xu, V. K. Anand, A. K. Bera, M. Frontzek, D. L. Abernathy, N. Casati, K. Siemensmeyer, and B. Lake, Magnetic structure and crystal-field states of the pyrochlore antiferromagnet $Nd_2Zr_2O_7$, Phys. Rev. B **92**, 224430 (2015).

[41] M. C. Hatnean, M. R. Lees, O. A. Petrenko, D. S. Keeble, G. Balakrishnan, M. J. Gutmann, V. V. Klekovkina, and B. Z. Malkin, Structural and magnetic investigations of single-crystalline neodymium zirconate pyrochlore $Nd_2Zr_2O_7$, Phys. Rev. B **91**, 174416 (2015).